Monthly Notices of the ROYAL ASTRONOMICAL SOCIETY

MNRAS **534,** 3853–3868 (2024) https://doi.org/10.1093/mnras/stae2289
Advance Access publication 2024 October 04

# Late-time supernovae radio re-brightening in the VAST pilot survey

Kovi Rose [1,2,3★] Assaf Horesh [1] Tara Murphy [2,4] David L. Kaplan [5] Itai Sfaradi,[1] Stuart D. Ryder [6,7] Robert J. Aloisi,[5,8] Dougal Dobie [2,4] Laura Driessen [2] Rob Fender,[9] David A. Green [10] James K. Leung [1,11,12] Emil Lenc [3] Hao Qiu [13] and David Williams-Baldwin [14]

[1]*Racah Institute of Physics, The Hebrew University of Jerusalem, Jerusalem 91904, Israel*
[2]*Sydney Institute for Astronomy, School of Physics, The University of Sydney, Camperdown, NSW 2006, Australia*
[3]*CSIRO Astronomy and Space Science, PO Box 76, Epping, NSW 1710, Australia*
[4]*ARC Centre of Excellence for Gravitational Wave Discovery (OzGrav), Hawthorn, VIC 3122, Australia*
[5]*Center for Gravitation, Cosmology, and Astrophysics, Department of Physics, University of Wisconsin–Milwaukee, PO Box 413, Milwaukee, WI 53201, USA*
[6]*School of Mathematical and Physical Sciences, Macquarie University, Sydney, NSW 2109, Australia*
[7]*Astrophysics and Space Technologies Research Centre, Macquarie University, Sydney, NSW 2109, Australia*
[8]*Department of Astronomy, University of Wisconsin-Madison, 475 North Charter Street, Madison, WI 53706, USA*
[9]*Astrophysics, Department of Physics, University of Oxford, Keble Road, Oxford OX1 3RH, UK*
[10]*Astrophysics Group, Cavendish Laboratory, 19 J. J. Thomson Ave, Cambridge CB3 0HE, UK*
[11]*David A. Dunlap Department of Astronomy and Astrophysics, University of Toronto, 50 St. George Street, Toronto, ON M5S 3H4, Canada*
[12]*Dunlap Institute for Astronomy and Astrophysics, University of Toronto, 50 St. George Street, Toronto, ON M5S 3H4, Canada*
[13]*SKA Observatory, Jodrell Bank, Lower Withington, Macclesfield, Cheshire SK11 9FT, UK*
[14]*Jodrell Bank Centre for Astrophysics, School of Physics and Astronomy, The University of Manchester, Manchester M13 9PL, UK*

Accepted 2024 October 1. Received 2024 October 1; in original form 2024 June 14

## ABSTRACT

We present our analysis of supernovae serendipitously found to be radio-bright several years after their optical discovery. We used recent observations from the Australian SKA Pathfinder (ASKAP) taken as part of the pilot Variables and Slow Transients and Rapid ASKAP Continuum Survey programmes. We identified 29 objects by cross-matching sources from these ASKAP observations with known core-collapse supernovae below a declination of $+40^{\circ}$ and with a redshift of $z \leq 0.15$. Our results focus on eight cases that show potential late-time radio emission. These supernovae exhibit significantly greater amounts of radio emission than expected from the standard model of a single shockwave propagating through a spherical circumstellar medium, with a constant density structure produced by regular stellar mass-loss. We also discuss how we can learn from future ASKAP surveys about the circumstellar environments and emission mechanisms of supernovae that undergo late-time radio re-brightening. This pilot work tested and confirmed the potential of the Variables and Slow Transients survey to discover and study late-time supernova emission.

**Key words:** circumstellar matter – gamma-ray burst: general – transients: supernovae – radio continuum: transients.

## 1 INTRODUCTION

Massive stars shed mass via different mechanisms throughout their evolution. It has been suggested that some massive stars undergo increasingly violent eruptions during the final stages of stellar evolution, releasing large amounts of mass ranging from $10^{-7}$ to $10^{-2}\,\mathrm{M}_{\odot}\,\mathrm{yr}^{-1}$ (e.g. Langer 2012; Smith 2014, and references therein). Stars with an initial mass of more than 8 $\mathrm{M}_{\odot}$ are generally expected to explode in an energetic astronomical event known as a core-collapse supernova (CCSN). CCSNe occur when massive stars exhaust their nuclear fuel and collapse inwards due to overwhelming gravitational forces (Heger et al. 2003).

The radio emission that we detect from CCSNe arises from a fast-moving outflow of the supernova (SN) ejecta – which may be relativistic or subrelativistic – interacting with the circumstellar medium (CSM) and driving a shockwave that amplifies the magnetic field and accelerates electrons in the surrounding environment (Chevalier 1982). In the post-shocked region, particles are accelerated to relativistic energies.

The spectrum of these relativistic electrons, as described by Chevalier (1998), has a power-law distribution given by $N(E) = N_0 E^{-\gamma}$, where $N$ is the number density of electrons, $N_0$ is a normalization constant, and $\gamma$ is the spectral index of the relativistic electron energy density. A small fraction of the post-shock energy goes into enhancing magnetic fields, which causes the gyration of relativistic electrons and produces the synchrotron emission (Chevalier 1996).

Some of these synchrotron photons can in turn be reabsorbed by nearby relativistic electrons in a process known as synchrotron self-absorption (SSA). Free–free absorption (FFA) – generated from free electrons decelerating and scattering off charged ions – can also modify the emitted radiation (e.g. Weiler et al. 2002). FFA generally

★ E-mail: kovi.rose@sydney.edu.au

only dominates the emission at early times or in cases of slow-moving shocks (e.g. Chevalier 1998; Margalit & Quataert 2024).

Modelling the radio emission enables us to probe the circumstellar or interstellar medium (ISM), derive physical parameters of the shock, and reveal the progenitor star's mass-loss history. Examples of this sort of parameter space exploration can be seen in the analyses conducted by Chevalier (1998), Wellons, Soderberg & Chevalier (2012), Horesh et al. (2020), Bietenholz et al. (2021), and others.

The standard model of a CSM with constant density structure is understood to be the result of constant mass-loss over thousands of years before the explosion. For relatively old SNe, radio observations provide a unique set of tools to examine the progenitor mass-loss variations over long time-scales. In contrast to the prompt emission usually detected within days or weeks of the optical discovery, the physical processes that generate comparable levels of radio emission many months or years after the supernova explodes are not as well understood. In most cases, the emission gradually fades over time as the shock loses energy and the CSM becomes more diffuse. However, there are instances where the radio emission is not monotonic, but brightens years after the SN.

Instances of such late-time radio re-brightening are rare but there are prominent cases like SN 2007bg (Salas et al. 2013), SN 2014C (Anderson et al. 2017), and PTF11qcj (Palliyaguru et al. 2021). These SNe exhibit a double peak in their radio light curves, showing two clear periods of re-brightening roughly $10^2$–$10^3$ d after their optical discovery. Analyses of these SNe (Salas et al. 2013; Anderson et al. 2017; Palliyaguru et al. 2021) support the interpretation of radio re-brightening caused by a propagating shock front interacting with two (or more) distinct CSM regions ejected prior to the explosion.

The rarity of late-time radio emission is partly due to the fact that most SNe are not followed up at late times after explosion. The same is true for tidal disruption events (TDEs) which have also been found to exhibit late-time radio re-brightening (e.g. Sfaradi et al. 2022; Anumarlapudi et al. 2024).

It is anticipated that wide-field all-sky radio surveys will produce more detections of re-brightening events. For example, the Karl G. Jansky Very Large Array (VLA; Perley et al. 2011) Sky Survey (VLASS; Lacy et al. 2020) – which covers $\sim 82$ per cent of the sky (33 885 deg$^2$) at 2–4 GHz – has identified new transients and late-time SNe re-brightening events (e.g. Stroh et al. 2021). VLASS has a typical root mean square (RMS) noise sensitivity of 0.12 mJy beam$^{-1}$. The Australian SKA Pathfinder (ASKAP; Hotan et al. 2021) telescope is an ideal instrument for detecting radio transients in the Southern hemisphere, with a large field of view and a typical RMS noise sensitivity $\sim 0.25$ mJy beam$^{-1}$ for a 15 min observation.

In this paper, we present our search for CCSNe that exhibit late-time radio re-brightening. In Section 2, we summarize the relevant ASKAP surveys and technical specifications, as well as the data reduction from follow-up observations. Section 3 describes the candidate selection process and our light-curve modelling and analysis. In Section 4, we present our findings for all of the sources of interest. Finally, in Section 5, we discuss the implications of our results regarding ASKAP and the detection of similar late-time emission from CCSNe.

## 2 OBSERVATIONS

### 2.1 ASKAP survey observations

ASKAP is located at Inyarrimanha Ilgari Bundara, the CSIRO's Murchison radio astronomy observatory in Western Australia. It is a radio telescope array comprised of 36 parabolic antennae. Each dish is 12 m in diameter and has a phased array feed that enables a large 30 deg$^2$ field of view. We used data from the rapid ASKAP continuum survey (RACS[1]; McConnell et al. 2020) and the variable and slow transients (VAST[2]; Murphy et al. 2013) survey. The observations from both surveys were reduced with the `ASKAPSoft` data reduction pipeline (Cornwell, Voronkov & Humphreys 2012), which uses daily observations of PKS B1934−638 for bandpass, flux-density scale, and on-axis leakage calibration. After initial calibration the pipeline runs imaging and self-calibration on the data from each of the beams; see Hotan et al. (2021) for further details. The SELAVY source-finding package (Whiting 2012) is implemented in `ASKAPSoft`. It produces catalogues of both extended and point sources by fitting Gaussian components to neighbouring pixels with a signal above a set detection threshold.

The first RACS data release (RACS-low; Hale et al. 2021) covers the sky south of $+41^\circ$ declination ($\sim 34\,240$ deg$^2$), observed between 2019 April and 2020 June with $\sim$15 min observations at a central frequency of 887.5 MHz and an angular resolution of 15 arcsec. We used the RACS-low source catalogue as the main survey for our cross-matching. The VAST Phase I Pilot Survey (VAST-P1; Murphy et al. 2021) has a total sky footprint of 5131 deg$^2$ with 12 min observations conducted between 2019 August and 2020 August at the same observing frequency. We used the VAST-P1 catalogue and other publicly available ASKAP observations as additional light-curve epochs, including data from the ongoing full VAST survey which covers an $\sim 9500$ deg$^2$ sky region at roughly a bimonthly cadence. To obtain the ASKAP flux uncertainties used in this work, we took the quadrature sum of the SELAVY peak flux error, image RMS, and a 6 per cent flux scaling error.

### 2.2 AMI–LA and ATCA follow-up observations

We conducted follow-up radio observations of selected sources with the Arcminute Microkelvin Imager–Large Array (AMI–LA; Zwart et al. 2008; Hickish et al. 2018) and the Australia Telescope Compact Array (ATCA; Wilson et al. 2011). The results of these observations are presented in Section 4 and the measurements are available in the supplementary material.

The data from AMI–LA were initially flagged and calibrated using REDUCE_DC, a customized data reduction software package (Perrott et al. 2013). We used the CASA (Common Astronomy Software Applications) package (McMullin et al. 2007) for additional flagging and imaging of the AMI–LA data, as well as the reduction of archival observations retrieved from the VLA Data Archive.[3] Observations from ATCA were reduced using the MIRIAD software package (Sault, Teuben & Wright 1995).

AMI–LA observes with a 5 GHz bandwidth around a central frequency of 15.5 GHz. We conducted two 4 h observations of SN 2004dk and one 4 h observation of SN 2012ap. Daily observations of 3C286 were used for absolute flux calibration, and short interleaved observations of the phase calibrators (J1620+0036 for SN 2004dk and J0501−0159 for SN 2012ap) were used for phase calibrations. Images of the SNe fields were produced by the CASA task `clean` in an interactive mode. The image RMS was calculated using the CASA task `imstat`, and the sources at the phase centres were fitted with the CASA task `imfit`. We estimated the uncertainty

[1] https://research.csiro.au/racs
[2] https://vast-survey.org
[3] https://archive.nrao.edu/archive/advquery.jsp

of the peak flux density to be a quadratic sum of the error produced by CASA task `imfit` and a 5 per cent calibration error.

We conducted eight observations of SN 2012dy with ATCA for a total of 39 h – with the project codes C3363 (PI: Murphy) and C3442 (PI: Horesh) – in *L*/*S* band (1.1–3.1 GHz) and simultaneously in *C* band (4.5–6.5 GHz) and *X* band (8.0–10.0 GHz). For all observations, we used the ATCA primary calibrator source PKS 1934−638 as the bandpass and flux calibrator, with the calibrator sources PKS 2117−642 and PKS 2204−540 for phase calibration scans in *L* band and *C*/*X* band, respectively. We used the MIRIAD software (Sault et al. 1995) to reduce and image the data, using `mfclean` with Briggs weighting and a `robust` parameter of 0.0, with multifrequency synthesis (`mfs`) deconvolution. We used the MIRIAD`imfit` routine to fit the point sources at the central frequencies for each full band (2.1, 5.5, 9.0 GHz). We calculated the uncertainties as the quadrature sum of the fitted error, the image RMS, and a 10 per cent flux scaling error.

## 3 METHODOLOGY

### 3.1 Sample selection

We compiled a list of known CCSNe – as of 2019 October – from a number of astronomical data bases in order to obtain a set of candidate CCSNe with late-time radio emission. This cut-off date was chosen because ASKAP had completed three observing epochs of all VAST-P1 fields by the end of 2019 October (see table 2 in Murphy et al. 2021). After removing 534 duplicate objects there were 10 700 CCSne including 3833 from the Transient Name Server[4] (Gal-Yam 2021), 3046 from the Asiago supernova catalogue[5] (Barbon et al. 1999), 500 from Wiserep[6] (Yaron & Gal-Yam 2012), 900 from the Sloan Digital Sky Survey (SDSS-II) supernova survey[7] (Frieman et al. 2008), and 2421 from the Set of Identifications, Measurements and Bibliography for Astronomical Data[8] (SIMBAD; Wenger et al. 2000).

From this collection of 10 700, we reduced the sample to 3658 CCSNe by filtering out objects with declinations $> +40^{\circ}$, retaining only Type II and Type Ib/c SNe, and removing sources with $z > 0.15$ or with unknown redshifts. This is because $z = 0.15$ represents the limiting distance ($\sim 700$ Mpc) for ASKAP to make a $5\sigma$ detection of three times the maximum peak luminosity for CCSNe at 887.5 MHz: $L_\nu \sim 10^{29}$ erg s$^{-1}$Hz$^{-1}$ – see Appendix A for the sensitivity limit calculation. On average most CCSNe have a much lower peak luminosity around $L_\nu \sim 10^{25.5}$ erg s$^{-1}$ Hz$^{-1}$ (Bietenholz et al. 2021) which, with the same calculation, would correspond to a distance of $\sim 8$ Mpc ($z = 0.002$). We cross-matched the sky coordinates of the 3658 CCSNe with sources in the RACS-low catalogue using a 15 arcsec match radius, finding matches for 29 CCSNe – see Appendix B for the complete candidate list.

We generated light curves of radio detections and limits for these 29 cross-matched CCSNe using data from VAST and RACS-low, as well as from archival surveys like the faint images of the radio sky at twenty-centimeters (FIRST; Becker, White & Helfand 1995) survey, the National Radio Astronomy Observatory VLA Sky Survey (NVSS; Condon et al. 1998), and VLASS. The NVSS and FIRST surveys were carried out at 1.4 GHz and have typical RMS sensitivities of 0.45 and 0.13 mJy beam$^{-1}$, respectively. These light curves, and the more comprehensive ones shown in Section 4, were generated relative to the optical discovery/explosion date found in the OpenSNe catalogue[9] (Guillochon et al. 2017).

We inspected these light curves, as well as radio image cutouts, and identified eight CCSNe with an ASKAP radio detection positionally offset from the nuclear region of the host galaxy: SN 1996aq, SN 2003bg, SN 2004dk, SN 2012ap, SN 2012dy, SN 2013bi, SN 2016coi, SN 2017gmr – see Table 1 for additional information. We selected these CCSNe as candidates for late-time re-brightening as the radio emission was detected $10^2$–$10^3$ d after their initial optical discovery. In the cases of SN 2012dy and SN 2013bi, the RACS-low observations were the first detections of radio emission from the sources.

There were a further six of the 29 cross-matched CCSNe which we also considered as potential candidates for late-time radio re-brightening: SN 2002hy, SN 2004gg, SN 2006O, SN 2008de, SN 2008fi, and SN 2017hyh. We did not include these sources in our analysis because the ASKAP detection appears to be contaminated by radio emission from host galaxy. We list these sources and the full sample of cross-matched CCSNe in Appendix B.

### 3.2 Modelling and analysis

To analyse the appearance and evolution of the radio re-brightening events presented in this work, we adopted the standard model of synchrotron emission (Chevalier 1982) which describes the interaction between the propagating SN shockwave and the surrounding material. We assume a CSM density $\rho_{\rm CSM} \propto r^{-s}$ that is constant in time, unlike the outer density profile of the SN which has a power-law $\rho_{\rm SN} \propto r^{-n}t^{n-3}$. Following Chevalier (1982), we require that $n > 5$. From Chevalier (1998), we adopt the expression for the radio flux density as a function of time and frequency:

$$F_\nu(t) = 1.582 F_{\nu_{\rm c}}(t_{\rm c}) \left(\frac{t}{t_{\rm c}}\right)^{a} \left(\frac{\nu}{\nu_{\rm c}}\right)^{5/2} \times \left(1 - \exp\left[-\left(\frac{t}{t_{\rm c}}\right)^{-(a+b)} \left(\frac{\nu}{\nu_{\rm c}}\right)^{-(\gamma+4)/2}\right]\right), \quad (1)$$

where $F_\nu \propto t^a$ is the power law in the optically thick regime; $F_\nu \propto t^{-b}$ is the power law in the optically thin regime; and $t_{\rm c}$, $\nu_{\rm c}$ are the peak time and frequency at which the emission transitions from optically thick to optically thin.

When the spectral peak is given, Chevalier (1998) provides the following equations to calculate the radius of a fast-moving shock $R_{\rm p}$ at the leading edge of the emitting region, as well its magnetic field strength $B_{\rm p}$:

$$R_{\rm p} = \left[\frac{6c_6{}^{\gamma+6} F_{\rm p}^{\gamma+6} D^{2\gamma+12}}{\alpha_\epsilon f(\gamma-2)\pi^{\gamma+5} c_5^{\gamma+6} E_1^{\gamma-2}}\right]^{1/(2\gamma+13)} \left(\frac{\nu}{2c_1}\right)^{-1}, \quad (2)$$

$$B_{\rm p} = \left[\frac{36\pi^3 c_5}{\alpha_\epsilon^2 f^2(\gamma-2)^2 c_6^3 E_1^{2(\gamma-2)} F_{\rm p} D^2}\right]^{2/(2\gamma+13)} \left(\frac{\nu}{2c_1}\right), \quad (3)$$

where $\alpha_\epsilon$ is the ratio of electron and magnetic energy densities, $D$ is the distance to the SN, $F_{\rm p}$ is the peak flux density, $\nu$ is the frequency, $f$ is the geometric filling factor for the emission, $E_1 = 0.51$ MeV is the electron rest energy, and $c_1$, $c_5$, $c_6$ are constants (see Appendix C).

In this work, we assume an equipartition of electron and magnetic energies $\epsilon_{\rm e} = \epsilon_{\rm B} = 0.1 \rightarrow \alpha_\epsilon = 1$ – although there have been a

[4] https://www.wis-tns.org/
[5] https://heasarc.gsfc.nasa.gov/W3Browse/all/asiagosn.html
[6] https://www.wiserep.org/
[7] http://classic.sdss.org/supernova/snlist_confirmed.html
[8] http://simbad.u-strasbg.fr/simbad
[9] https://sne.space/

**Table 1.** Primary CCSNe candidates for late-time radio re-brightening identified and analysed for this work. The type, redshift, discovery date, and distance are taken from the OpenSNe catalogue. The classification column refers to the category of re-brightening: a re-brightening event due to interaction with a single CSM shell, variability due to interaction with CSM structure or other intrinsic processes, or refractive scintillation. We do not provide a classification for SN 2013bi due to the lack of detections. The variability of SN 2017gmr is consistent with scintillation but more data are required to conclusively classify the variability.

| Name | Type | RA | Dec. | Redshift | Disc. (MJD) | Dist. (Mpc) | Classification |
|---|---|---|---|---|---|---|---|
| SN 1996aq | SN Ic | 14:22:22.7 | −00:23:23 | 0.0055 | 50312 | 23.9 | Variability |
| SN 2003bg | SN IIb | 04:10:59.4 | −31:24:49 | 0.0045 | 52695 | 19.5 | Re-brightening |
| SN 2004dk | SN Ib | 16:21:48.9 | −02:16:17 | 0.0052 | 53216 | 22.6 | Re-brightening |
| SN 2012ap | SN Ic-BL | 05:00:13.7 | −03:20:50 | 0.012 | 55967 | 53.3 | Variability |
| SN 2012dy | SN II | 21:18:50.7 | −57:38:42 | 0.0104 | 56142 | 45.3 | Re-brightening |
| SN 2013bi | SN IIp | 18:25:02.1 | +27:31:53 | 0.016 | 56375 | 69.6 | – |
| SN 2016coi | SN Ic-BL | 21:59:04.1 | +18:11:11 | 0.0036 | 57535 | 15.6 | Variability |
| SN 2017gmr | SN II | 02:35:30.2 | −09:21:14 | 0.005 | 58000 | 21.7 | Scintillation |

**Table 2.** The brightest radio detections of each SN in our sample. We use the peak flux densities and observing frequencies to obtain limits on the radius of the emission region, as well as the magnetic field strength, CSM density, number density, and shock velocity. These peak flux densities are a limit on the spectral peak, meaning that the true peak flux density should be higher and the true peak frequency lower. The brightest measurements for five of the eight SNe in this sample come from late-time ($\Delta t > 10^3$ d) emission, four of which were detected with ASKAP. Detections at 0.887 and 0.855 GHz are from ASKAP with the other detections observed with the VLA.

| Name | $\Delta t$ (d) | $F_\nu$ (mJy beam$^{-1}$) | $\nu$ (GHz) | $L_\nu$ (erg s$^{-1}$ Hz$^{-1}$) | $R_\mathrm{p}$ (cm) | $B_\mathrm{p}$ (G) | $\rho_\mathrm{CSM}$ (g cm$^{-3}$) | $n_\mathrm{p}$ (cm$^{-3}$) | $v_\mathrm{sh}$ (km s$^{-1}$) |
|---|---|---|---|---|---|---|---|---|---|
| SN 1996aq | 8648 | $3.17 \pm 0.28$ | 0.855 | $\sim 1.4 \times 10^{27}$ | $\gtrsim 5.4 \times 10^{16}$ | $\lesssim 0.097$ | $\approx 6.2 \times 10^{-19}$ | $\approx 3.7 \times 10^{5}$ | $\approx 730$ |
| SN 2003bg | 23 | $106.3 \pm 2.2$ | 22.5 | $\sim 5.2 \times 10^{28}$ | $\gtrsim 1.2 \times 10^{16}$ | $\lesssim 1.7$ | $\approx 3.1 \times 10^{-20}$ | $\approx 1.9 \times 10^{3}$ | $\approx 58\,000$ |
| SN 2004dk | 5994 | $21.53 \pm 4.31$ | 0.34 | $\sim 4.5 \times 10^{26}$ | $\gtrsim 8.1 \times 10^{16}$ | $\lesssim 0.043$ | $\approx 2.7 \times 10^{-20}$ | $\approx 1.6 \times 10^{4}$ | $\approx 1500$ |
| SN 2012ap | 4279 | $10.98 \pm 1.08$ | 0.887 | $\sim 3.9 \times 10^{28}$ | $\gtrsim 2.6 \times 10^{17}$ | $\lesssim 0.071$ | $\approx 3.6 \times 10^{-21}$ | $\approx 2.1 \times 10^{3}$ | $\approx 7000$ |
| SN 2012dy | 2580 | $18.37 \pm 1.12$ | 0.887 | $\sim 4.6 \times 10^{28}$ | $\gtrsim 2.8 \times 10^{17}$ | $\lesssim 0.069$ | $\approx 1.1 \times 10^{-21}$ | $\approx 6.5 \times 10^{2}$ | $\approx 13\,000$ |
| SN 2013bi | 2595 | $4.73 \pm 0.41$ | 0.887 | $\sim 2.9 \times 10^{28}$ | $\gtrsim 2.2 \times 10^{17}$ | $\lesssim 0.073$ | $\approx 1.9 \times 10^{-21}$ | $\approx 1.1 \times 10^{3}$ | $\approx 10\,000$ |
| SN 2016coi | 21 | $24.0 \pm 1.0$ | 21.85 | $\sim 7.5 \times 10^{27}$ | $\gtrsim 4.8 \times 10^{15}$ | $\lesssim 2.08$ | $\approx 2.2 \times 10^{-19}$ | $\approx 1.3 \times 10^{5}$ | $\approx 26\,000$ |
| SN 2017gmr | 858 | $1.89 \pm 0.39$ | 0.887 | $\sim 1.1 \times 10^{27}$ | $\gtrsim 4.8 \times 10^{16}$ | $\lesssim 0.10$ | $\approx 8.8 \times 10^{-21}$ | $\approx 5.3 \times 10^{3}$ | $\approx 6500$ |

number of recent examples of deviation from equipartition (e.g. Horesh et al. 2020; Ruiz-Carmona, Sfaradi & Horesh 2022). We also assume an emission filling factor $f = 0.5$, and an electron energy spectral index $\gamma = 3$.

The shock radius can be used to calculate the mean shock velocity as $v_\mathrm{sh} = R_\mathrm{p}/t$. A typical assumption is that the magnetic energy density, $B^2/8\pi$, is a fraction, $\epsilon_\mathrm{B}$, of the post-shock energy density, $\frac{9}{8}\rho_\mathrm{CSM} v_\mathrm{sh}^2$. In the case of a constant mass-loss in a steady wind $v_\mathrm{w}$, as is often assumed in the CSM interaction model, we can define CSM density simply as:

$$\rho_\mathrm{CSM} = \frac{\dot{M}}{4\pi r^2 v_\mathrm{w}}. \tag{4}$$

This results in the mass-loss rate:

$$\dot{M} = 5.2 \times 10^{-7} \left(\frac{\epsilon_\mathrm{B}}{0.1}\right)^{-1} \left(\frac{B}{1\,\mathrm{G}}\right)^2 \times \left(\frac{t}{10\,\mathrm{d}}\right)^2 \left(\frac{v_\mathrm{w}}{100\,\mathrm{km\ s^{-1}}}\right) \mathrm{M_\odot\ yr^{-1}} \tag{5}$$

which we can calculate for a range of wind velocities $v_\mathrm{w}$ as part of our general investigation into the physical properties of the circumstellar region. For our calculations, we use the wind velocities 10 and 1000 km s$^{-1}$ for Type II and Type Ib/c SNe, respectively (Smith 2014).

We use the EMCEE Python package (Foreman-Mackey et al. 2013) to implement a Markov chain Monte Carlo (MCMC) sampler and fit the observations to the Chevalier (1998) model. We used 100 walkers and a burn-in period of 1000 iterations. For our model, we used the more general form of equation (1) to include a full parametrization of the multifrequency data

$$F_\nu(t) = 1.582 F_{\nu_\mathrm{c}}(t_\mathrm{c}) \left(\frac{t}{t_\mathrm{c}}\right)^a \left(\frac{\nu}{\nu_\mathrm{c}}\right)^\alpha \times \left(1 - \exp\left[-\left(\frac{t}{t_\mathrm{c}}\right)^{-(a+b)} \left(\frac{\nu}{\nu_\mathrm{c}}\right)^{-(\alpha+\beta)}\right]\right) \tag{6}$$

assuming a peak frequency of 887.5 MHz.

This model is applied to SNe which produced detectable radio emission at early times, using a $\chi^2$ log likelihood function

$$\log\left[\mathcal{L}(F|\theta, t, \delta F)\right] = -\frac{1}{2}\sum\left(\frac{F - F_\nu(t,\theta)}{\sqrt{\delta F}}\right)^2, \tag{7}$$

where $F$ is the flux density measurement, $\delta F$ the flux density errors, and $\theta$ the parameters $F_\mathrm{p}$, $t_\mathrm{p}$, $\alpha$, $\beta$, $a$, and $b$. We use flat prior distributions for these parameters, over the following prior ranges: $10^{-2} < F_\mathrm{p} < 10^2$; $10^{-1} < t_\mathrm{p} < 2 \times 10^4$; $-5.0 < \alpha < 5.0$; $-5.0 < \beta < 5.0$; $-5.0 < a < 5.0$; $-5.0 < b < 5.0$. For further details about the MCMC algorithm, see Foreman-Mackey et al. (2013).

We fit the multifrequency data from $\Delta t < 3 \times 10^3$ d. We do not fit this model to the SNe with few or no radio detections within the first $\sim 10^2$ d after optical discovery.

For all SNe we also extract astrophysical parameters of the shock and surrounding medium, making the simplifying assumption that the peak in the light curve follows the transition of the shock from an optically thick to an optically thin region – using equations (2), (3), and (5). We discuss the validity of this assumption in Section 5.

We also quantify the variability of the emission using the modulation index

$$V = \frac{1}{\langle F \rangle} \sqrt{\frac{N}{N-1} \langle F^2 \rangle - \langle F \rangle^2} \tag{8}$$

and the reduced $\chi^2$ parameter (relative to a constant model)

$$\eta = \frac{N}{N-1} \left( \langle w F^2 \rangle \frac{\langle w F \rangle^2}{\langle w \rangle} \right), \tag{9}$$

where $N$ is the number of measurements and $w_i = 1/\sigma_i^2$ is the measurement weight defined with $\sigma_i$ being the uncertainty corresponding to the $i$-th measurement. We use $\langle\rangle$ to denote the arithmetic mean of a value across the measurements. The $V$, $\eta$ metrics provide measures of the degree and significance of the variability, respectively.

For comparison, we also calculate the expected variability index $m$ caused by refractive interstellar scintillation (RISS) at 887.5 MHz, assuming a scattering screen at a distance of 1 Mpc. For this, we use the RISS19 package (Hancock et al. 2019). For observations at 887.5 MHz – or generally $\leq$ 1 GHz – extragalactic sources like SNe are in the strong scattering regime. In this regime, RISS produces lower variation in time compared to diffractive scintillation, which is uncommon in extragalactic radio sources (Hancock et al. 2019).

## 4 RESULTS

In this section, we describe the results from our review of the CCSNe that were found to be sources potentially undergoing periods of late-time radio re-brightening. Besides the data bases (see Section 3.1), our archival review included a thorough search for reported emission at optical, radio, or X-ray wavelengths in the literature – Astrophysics Data System[10] and Astronomer's Telegram[11] – as well as in the archives of NASA/IPAC Extragalactic Database[12], High Energy Astrophysics Science Archive Research Center,[13] Panoramic Survey Telescope And Rapid Response System,[14] VLASS,[15] CSIRO ASKAP Science Data Archive (CASDA[16]), and Australia Telescope Online Archive (ATOA[17]). One motivation for this search was to demonstrate the role of ASKAP to commensally study the late-time evolution of CCSNe and detect new CCSNe re-brightening events.

### 4.1 SN 1996aq

SN 1996aq was discovered and classified as an SN Ic by Nakano et al. (1996) but was not detected in radio until 2009. It was observed in the *C* and *X* bands (4.9 GHz, 8.5 GHz) by Stockdale et al. (2009) with the VLA and with the Giant Metrewave Radio Telescope (GMRT) at 617 MHz (Chakraborti, Chandra & Ray 2009). More recently SN 1996aq has been detected in the *L*/*S* bands with the VLA (Project Code:16A-210), VLASS (Gordon et al. 2020), RACS-low, and multiple epochs of VAST-P1.

We searched archival NVSS and FIRST observations for host emission or other contaminating radio sources near the SN coordinates. These observations were taken at $\Delta t = -538$ d and $\Delta t = +720$ d, respectively relative to the optical discovery, and were both observed at a central frequency of 1.4 GHz. There is no emission detected within 5 arcsec of SN 1996aq in either observation, with a $5\sigma$ limit 0.735 mJy in the case of FIRST. By contrast the SN was detected with the VLA at 1.4 GHz with a flux density of $1.89 \pm 0.06$ mJy on $\Delta t = +7\,258$ d. This VLA detection, offset by $< 1$ arcsec from the SN coordinates, confirms that it is indeed SN 1996aq, and not one of the nearby radio sources, that is producing this increased radio flux density.

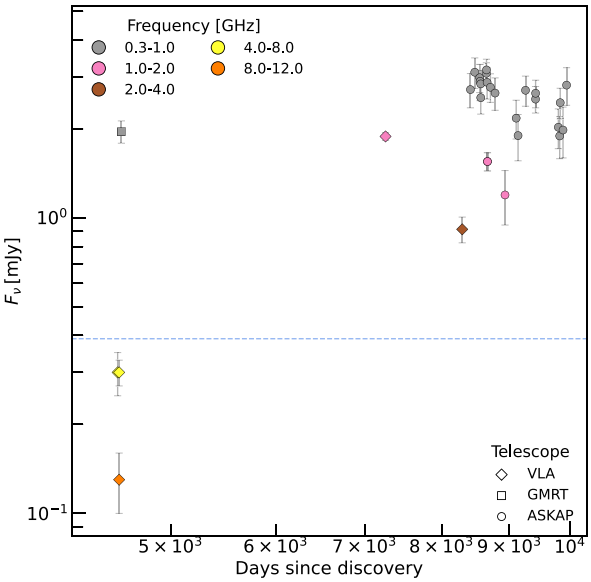


**Figure 1.** Radio detections of SN 1996aq from the literature and CASDA, including all public ASKAP observations as of 2023 December, binned into frequency bins and coloured accordingly. We use diamond markers for VLA detections, squares for GMRT, and circles for ASKAP. The dashed line represents the FIRST $3\sigma$ limit for any potential confusing host emission.

We used the equations given in Section 3.2 with the peak ASKAP flux density measurement of $F_p = 3.17 \pm 0.28$ mJy beam$^{-1}$ at 855.5 MHz from $\Delta t = 8\,648$ d. We calculate a lower limit on the shock radius to be $R_p \gtrsim 5.4 \times 10^{16}$ cm and an upper limit on the magnetic field strength of $B_p \lesssim 0.097$ G – using equations (2) and (3)å.

We list the calculated values for SN 1996aq, and for the other seven CCSNe in our sample, in Table 2. Assuming that the emission is optically thin, we use equation (5) to calculate the mass-loss rate. Assuming a wind velocity of $v_w = 1000$ km s$^{-1}$ (see Section 3.2) we find that it would require a CSM density of $\rho_{CSM} \approx 6.2 \times 10^{-19}$ g cm$^{-3}$ and a mean shockwave velocity $v_{sh} \approx 730$ km s$^{-1}$. We use the shock radius $R_p$ with the time $\Delta t$ to calculate this mean shockwave velocity – see Table 2 for values. Since the Chevalier (1998) equations are only valid in the high-velocity regime, there is some theoretical uncertainty in the values obtained for $B_p$ and $R_p$. There are additional theoretical uncertainties in the calculated values from the assumptions of our equipartition model – see Section 3.2 – as well as the measurement uncertainties.

By comparing flux densities from RACS-low and VLASS – extracting a flux density with the CASA`imfit` task – we obtained a spectral index of $\alpha = -0.91$. From Fig. 1, we can see that SN 1996aq is in the midst of a clear period of late-time re-brightening. We found that the variability of this re-brightening over time is not consistent with a power law.

[10] https://ui.adsabs.harvard.edu/
[11] https://www.astronomerstelegram.org/
[12] https://ned.ipac.caltech.edu/
[13] https://heasarc.gsfc.nasa.gov/
[14] https://ps1images.stsci.edu/cgi-bin/ps1cutouts
[15] http://cutouts.cirada.ca/
[16] https://data.csiro.au/collections/domain/casdaObservation/search/
[17] https://atoa.atnf.csiro.au/query.jsp

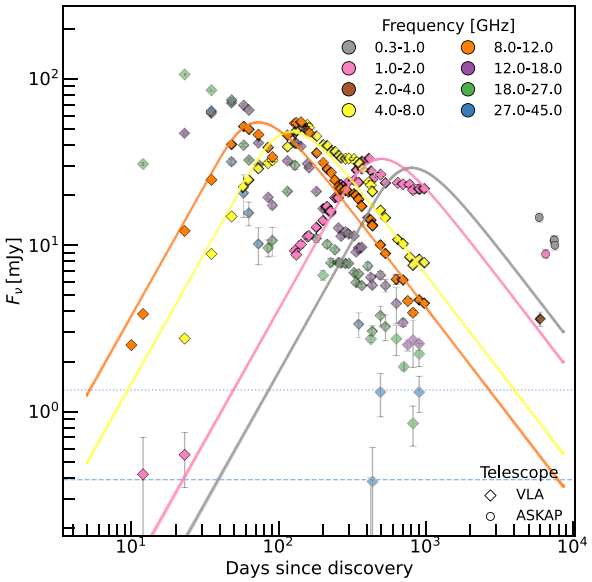


**Figure 2.** We show the archival radio detections of SN 2003bg (Soderberg et al. 2006; Gordon et al. 2020) along with the modelled light curves obtained from fitting of the early-time ($\Delta t < 10^3$ d) data. We also plot detections from all public ASKAP observations as of 2023 December. The MCMC parametrized light curves are extrapolated from the multifrequency data and plotted for 0.8875, 1.4, 5.5, 9.0 GHz. The data binned into frequency bins and coloured accordingly. We use diamond markers for VLA detections and circles for ASKAP. The dashed and dotted lines represent the FIRST and NVSS $3\sigma$ limits, respectively, for any potential confusing host emission.

### 4.2 SN 2003bg

SN 2003bg was discovered by Wood-Vasey et al. (2003) and within a year its spectral features had evolved, resulting in a reclassification from an SN Ic to an SN IIb hypernova (Hamuy et al. 2009; Mazzali et al. 2009). Based on variability in the radio light curve, it was suggested that this transition was due to CSM interaction (Soderberg et al. 2006).

Moriya, Groh & Meynet (2013) suggested that the radio emission from SN 2003bg may not be undergoing re-brightening but rather may be the modulated tail-end from the prompt emission decaying to lower frequencies – noting its similarity to SN 2001ig (Ryder et al. 2004). Similar comparisons were drawn to SN 2011ei by Milisavljevic et al. (2013), who suggested a two-component emission model to explain the deviation from an expected power-law decay in flux.

The early-time data for SN 2003bg fit the Chevalier (1998) model – see Fig. 2 – including a possible break in the decline shortly after the spectral turnover. We provide the fitted parameters in Table 3 and the MCMC posterior distributions corner plots in Appendix D. Based on our modelling it appears that the observed RACS emission is $\sim 5\times$ brighter than would be expected from the tail of the prompt emission. The same is true for the available VLASS measurement of SN 2003bg, which is a factor of $\sim 3\times$ brighter than the extrapolated value.

While a two-component model may provide a good fit with the early-time data – see Soderberg et al. (2006) – it does not explain the significant late-time re-brightening. Further observation and modelling of this SN may provide insights into density enhancements in the circumstellar region following pre-eruption mass-loss episodes.

### 4.3 SN 2004dk

SN 2004dk was one of the better-studied CCSNe in our sample, with multiple VLA observations of the region from the periods before and shortly after its discovery by Rajala et al. (2005), who classified it as an SN Ib. Wellons et al. (2012) were the first to identify the re-brightening of SN 2004dk and subsequent spectral analyses have noted the initial interaction with the hydrogen-rich CSM occurred $\Delta t \sim 1660$ d after discovery. Optical spectroscopy conducted by Mauerhan et al. (2018) at 4684 d confirmed that the interaction with the H-rich CSM was ongoing.

Balasubramanian et al. (2021) also reported the radio re-brightening of SN 2004dk at low frequencies (340 MHz) with the VLA low-band ionosphere and transient experiment (Clarke et al. 2016) – around the same time that RACS-low detected the SN. We conducted follow-up observations with AMI–LA and detected $2.85 \pm 0.21$ mJy beam$^{-1}$ peak flux density and $4.67 \pm 0.46$ mJy integrated flux density at 15.5 GHz. This emission is $\sim 3\times$ brighter than the 15 GHz VLA observations from $\Delta t = 33$ d (Wellons et al. 2012). We also see an order of magnitude increase in the VLA *C*- and *X*-band emission after $\Delta t \sim 10^3$ d, as well as a similar increase in the 1–2 GHz emission at late times compared to the NVSS $3\sigma$ limit – see Fig. 3.

The light-curve evolution and re-brightening of SN 2004dk presented in Fig. 3 appears similar to that of SN 2014C, which has been modelled as the late-time interaction of the SN shock with a dense circumstellar shell comprised of material from a previously stripped envelope (Anderson et al. 2017).

### 4.4 SN 2012ap

Following the discovery of SN 2012ap (Jewett et al. 2012), a number of groups reported on the optical spectroscopy and photometry in the first 100–272 d, and its classification as a SN Ic-BL (Milisavljevic et al. 2015; Prentice et al. 2016).

Early-time VLA detections showed the peak frequency shift from $11.82 \pm 0.48$ to $4.54 \pm 0.10$ GHz within $\Delta t = 38$ d of discovery (see table 1, Chakraborti et al. 2015). Over that same period, the corresponding peak flux densities declined from $5.85 \pm 0.58$ to $4.20 \pm 0.10$ mJy. This decay can be explained by the standard SSA emission mechanism (Chevalier 1998) but Chakraborti et al. (2015) noted that the evolution occurred much faster than other SNe Ibc. They calculated a lower limit of $0.4c$ on the initial expansion velocity, suggesting that there may have been an associated gamma-ray burst (GRB), though none was found.

We have since seen with VLASS (Gordon et al. 2020) and RACS-low that the peak frequency has continued to evolve more slowly at later times, as seen in Fig. 4. This is reasonable considering the deceleration of the shock that would occur while sweeping up additional mass as it propagates through the CSM and into the ISM.

Following early VLA and GMRT observations, Chakraborti et al. (2015) noted that SN 2012ap represented the first case of an SN with rapidly decelerating mildly relativistic ejecta but without a coincident GRB; there has only been one other SN with relativistic ejecta without an associated GRB (Soderberg et al. 2010).

Consequently a VLASS study (Stroh et al. 2021) – which also included the sources SN 2003bg, SN 2004dk, and SN 2016coi in their sample – suggested that, aside from the CSM interaction emission mechanism, the late-time radio re-brightening seen in SN 2012ap could be generated by an off-axis jet and cocoon; we note that this

**Table 3.** Chevalier (1998) model parameters for early-time emission. For each of the fitted CCSNe, we give the posteriors estimated with MCMC. We fit the early-time data – $\Delta t < 10^3$ d for SN 2003bg and $\Delta t < 3 \times 10^3$ d for SN 2004dk and SN 2016coi – with the free parameters $\alpha$, $\beta$ – see equation (6). These are the exponents for frequency-dependent terms with $\alpha$ and $\alpha + \beta$, in place of 5/2 and $(\gamma + 4)/2$ in equation (1). This $\alpha$ is unrelated to the $\alpha_\epsilon$ used to denote the energy density ratio in equations (2) and (3). The archival flux density measurement uncertainties used in the MCMC fit are taken from the literature – see Section 2 for the calibration uncertainties included for data from ATCA, AMI–LA, and ASKAP. See Appendix D for corresponding posterior distribution corner plots.

| Name | $F_p$ | $t_p$ | $\alpha$ | $\beta$ | $a$ | $b$ |
|---|---|---|---|---|---|---|
| SN 2003bg | $29.16^{+0.14}_{-0.14}$ | $804.75^{+5.04}_{-4.96}$ | $1.91^{+0.01}_{-0.01}$ | $0.92^{+0.004}_{-0.004}$ | $1.58^{+0.01}_{-0.01}$ | $1.15^{+0.004}_{-0.004}$ |
| SN 2004dk | $0.40^{+0.04}_{-0.03}$ | $80.16^{+10.93}_{-10.08}$ | $3.82^{+0.38}_{-0.31}$ | $-0.11^{+0.05}_{-0.06}$ | $3.25^{+0.43}_{-0.36}$ | $0.58^{+0.02}_{-0.02}$ |
| SN 2016coi | $11.02^{+0.37}_{-0.36}$ | $456.48^{+15.73}_{-15.55}$ | $2.13^{+0.05}_{-0.05}$ | $0.87^{+0.03}_{-0.03}$ | $1.81^{+0.04}_{-0.04}$ | $1.12^{+0.03}_{-0.03}$ |

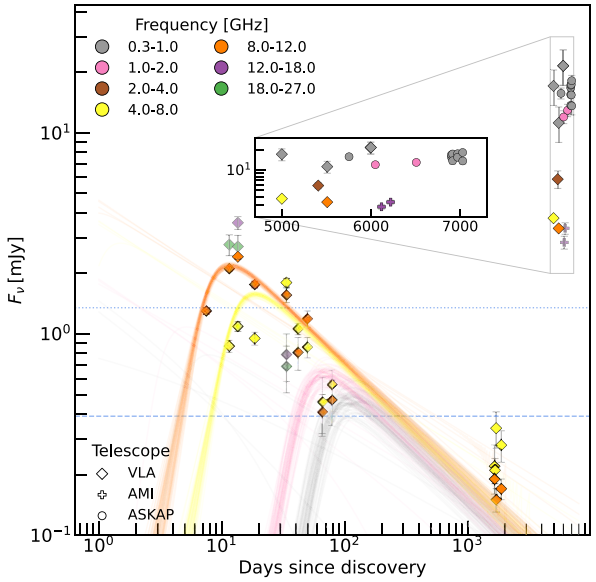


**Figure 3.** We show the archival radio detections of SN 2004dk (Wellons et al. 2012; Balasubramanian et al. 2021) along the modelled light curves obtained from fitting of the early-time ($\Delta t < 3 \times 10^3$ d) data. We also plot detections from all public ASKAP observations as of 2023 December. The MCMC parametrized light curves are extrapolated from the multifrequency data and plotted for 0.8875, 1.4, 5.5, 9.0 GHz, with the data binned into frequency bins and coloured accordingly. The inset shows a zoomed version of the late-time ($\Delta t > 3 \times 10^3$ d) data. We use diamond markers for VLA detections, pluses for AMI–LA, and circles for ASKAP. The dashed and dotted lines represent the FIRST and NVSS $3\sigma$ limits, respectively, for any potential confusing host emission.

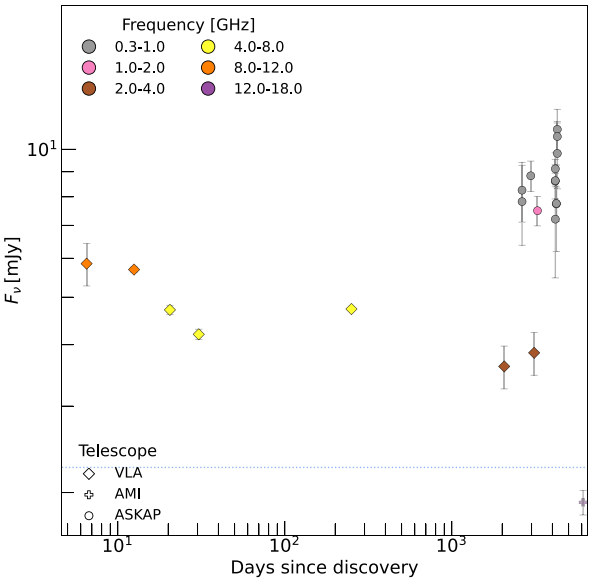


**Figure 4.** Archival radio detections of SN 2012ap from the literature (Chakraborti et al. 2015; Gordon et al. 2020) and CASDA, including all public ASKAP observations as of 2023 December, binned into frequency bins and coloured accordingly. We use diamond markers for VLA detections, pluses for AMI–LA, and circles for ASKAP. The dotted line represents the NVSS $5\sigma$ limit for any potential confusing host emission.

would be the first evidence of such a system from a massive stellar explosion.

Stroh et al. (2021) reported a clear VLASS detection coincident with the optical SN position – with no host emission – and our follow-up observation with AMI–LA detected a clear source of emission uncontaminated by emission from nearby sources. We used archival NVSS data for reference.

### 4.5 SN 2012dy

After its initial discovery by a member of the Backyard Observatory Supernova Search team (Bock et al. 2012), SN 2012dy was classified as a SN IIb by the Public European Southern Observatory Spectroscopic Survey of Transient Objects (PESSTO; Smartt et al. 2015). PESSTO spectra taken at weekly intervals over ∼140 d after discovery show the development of broad [O I], Si II, Ca II, and [Ca II] emission features, which is indicative of CSM interaction. Following this there were no observations of the object nor its host galaxy at any wavelength until ∼ 8 yr later when we first detected SN 2012dy with ASKAP.

Given the flux density variability of the source observed across RACS-low and several VAST-P1 epochs – see in Fig. 5 where RACS-low is the first radio detection of this SN – we conducted follow-up observations with ATCA under an existing VAST NAPA proposal (C3363). ASKAP and ATCA are the only telescopes to have detected this SN 2012dy at radio wavelengths because of its southern declination.

The emission revealed variability – showing indications of multiple peaks – with rapid evolution unlike any other radio SN observed so far. We also conducted further ATCA follow-up observations of SN 2012dy as part of a targeted new monitoring campaign (C3442) to study this unique temporal and spectral evolution. We split each of the three bands into four sub-bands (512 MHz bandwidth) and repeated this imaging process in order to derive the spectral index – see Table 4.

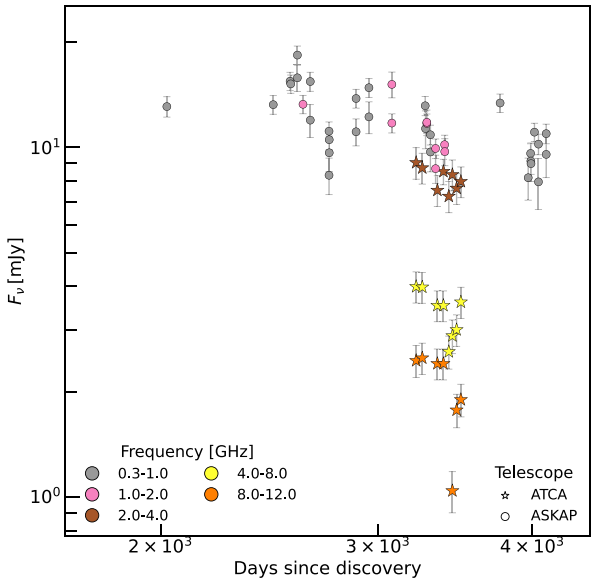


**Figure 5.** Radio detections of SN 2012dy from our ATCA observations and all public ASKAP data as of 2023 December, binned into frequency bins and coloured accordingly. We use circle markers for ASKAP detections and stars for ATCA.

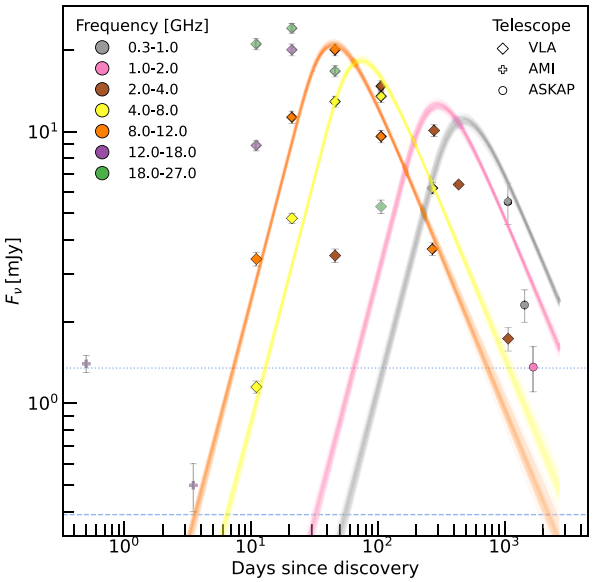


**Figure 6.** Archival radio detections of SN 2016coi (Mooley et al. 2016b; Terreran et al. 2019; Balasubramanian et al. 2021) along with the modelled light curves obtained from fitting of the early-time ($\Delta t < 3 \times 10^3$ d) data. We also plot detections from all public ASKAP observations as of 2023 December. The MCMC parametrized light curves are extrapolated from the multifrequency data and plotted for 0.8875, 1.4, 5.5, 9.0 GHz. The data binned into frequency bins and coloured accordingly. We use diamond markers for VLA detections and circles for ASKAP. The dashed and dotted blue lines represent the FIRST and NVSS $3\sigma$ limits – for any potential confusing host emission – respectively.

**Table 4.** We fit a power-law $F(\nu) = F_0(\nu/\nu_0)^{\alpha_{\rm fit}}$ to the SN 2012dy ATCA observations centred at 2.1, 5.5, 9.0 GHz to extrapolate the expected flux density $F_{\rm ex}$ at 0.8875 GHz. The observation on $\Delta t = 3422$ only includes the bands centred at 2.1, 5.5 GHz.

| $\Delta t$ (d) | $\alpha_{\rm fit}$ | $\nu_0$ (GHz) | $F_0$ (mJy) | $F_{\rm ex}$ (mJy) |
|---|---|---|---|---|
| 3220 | −0.87 | 1.49 | 11.66 | 18.30 |
| 3257 | −0.81 | 1.49 | 11.11 | 16.90 |
| 3350 | −0.79 | 1.47 | 10.52 | 15.71 |
| 3388 | −0.84 | 1.50 | 11.05 | 17.13 |
| 3422 | −0.97 | 1.46 | 10.20 | 16.54 |
| 3445 | −1.00 | 1.26 | 10.10 | 14.38 |
| 3472 | −0.96 | 1.54 | 10.39 | 17.71 |
| 3500 | −0.93 | 1.55 | 10.34 | 17.32 |

### 4.6 SN 2016coi

SN 2016coi was well studied in the year following its optical discovery (Grupe et al. 2016). There are a number of ATCA observations during the first ∼200 d (ATOA Projects C3142, CX363) and several observations within the first ∼ 274 d with the VLA.

The VLA observations were conducted by Terreran et al. (2019) whose subsequent analyses suggested a period of high mass-loss in the ∼ 30 yr prior to the explosion. They inferred a shockwave moving at $v_{\rm sh} \sim 0.15c$ which has since propagated into the dense surrounding medium.

SN 2016coi was detected at late times by RACS-low and VLASS – see Fig. 6 – providing a complementary point of reference to see the decaying peak emission frequency. Like SN 2003bg it is unclear whether there is a singular rising radio re-brightening event or if we are observing minor variability as part of secular light-curve decay. While both are likely the result of the shockwave interaction with the CSM structure, significant CSM density enhancements or shells would be necessary to produce an order of magnitude rise in radio flux density.

### 4.7 SN 2017gmr

SN 2017gmr was discovered by Valenti et al. (2017) and classified as an SN II (Pursimo et al. 2017). Photometric and spectral analyses of early-time data found evidence of CSM interaction and an asymmetric SN explosion (Andrews et al. 2019; Nagao et al. 2019). There are no radio observations of SN 2017gmr during the first ∼2 yr post-discovery.

The detection of radio emission at late times could indicate a re-brightening event – see Fig. 7 – but the emission appears to be consistent over nearly a year, as well as being quite close to the $5\sigma$ limit for both the FIRST and SELAVY source detection thresholds. Further observations are required to confirm whether there is any variability associated with this re-brightening. SN 2017gmr provides a good example of the types of potential false positives which must be correctly identified by future variability surveys and transient detection pipelines.

## 5 DISCUSSION

### 5.1 Variability & scintillation

The variability metrics shown in equations (8) and (9) are another way to identify false positives. We compared the calculated RISS variability indices, $m$, with the observed modulation metrics, $V$ and $\eta$, for these eight CCSNe – summarized in Table 5. The variability metrics are calculated using the 887.5 MHz VAST data from $\Delta t > 10^3$ d. We found that the observed late-time variability may not be the result of intrinsic variability of SN 1996aq and SN 2012ap, since $m \sim V$ and the signficance $\eta$ is low. For SN 2003bg and SN 2012dy, the observed late-time variability may be the result of intrinsic source variability

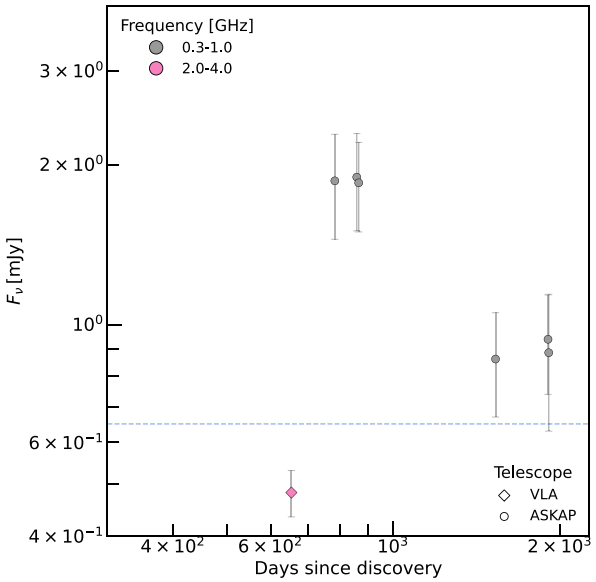


**Figure 7.** Archival radio detections of SN 2017gmr from the literature (Gordon et al. 2020) and CASDA, including all public ASKAP observations as of 2023 December, binned into frequency bins and coloured accordingly. We use diamond markers for VLA detections and circles for ASKAP. The dashed line represents the FIRST $5\sigma$ limit for any potential confusing host emission.

**Table 5.** The modulation index $V$ and the reduced $\chi^2$ metric $\eta$ calculated for the 887.5 MHz ASKAP data. $m$ is the index of expected RISS variability at this frequency (see Section 3.2). We do not calculate the $V$, $\eta$ variability metrics for SN 2013bi due to a paucity of detections. For SN 2016coi, there are only two 887.5 MHz ASKAP data points used to calculate these indices.

| Name | $m$ | $V$ | $\eta$ |
|---|---|---|---|
| SN 1996aq | 0.144 | 0.168 | 1.582 |
| SN 2003bg | 0.115 | 0.186 | 6.422 |
| SN 2004dk | 0.131 | 0.1 | 1.619 |
| SN 2012ap | 0.129 | 0.134 | 1.367 |
| SN 2012dy | 0.134 | 0.231 | 6.722 |
| SN 2013bi | 0.12 | – | – |
| SN 2016coi | 0.123 | 0.58 | 10.161 |
| SN 2017gmr | 0.139 | 0.012 | 0.004 |

as $m < V$ and $1 < \eta$. For these CCSNe, the variability is likely due to the interaction of the shock with a complex CSM structure. Similarly, while the variability at 887.5 MHz may be explained by refractive scintillation, RISS cannot account for the order of magnitude re-brightening of SN 2004dk at higher frequencies. This suggests that variability metrics alone cannot provide a definitive measure of whether or not a CCSNe is undergoing a period of late-time radio re-brightening. The variability of SN 2016coi also appears to be the result of an intrinsic change in the SN, with the decline in flux density relative to the modelled emission suggesting a drop in CSM density. For SN 2017gmr $m \gg V$ and the observed late-time emission is therefore consistent with extrinsic scintillation and not variability of the source, but more observations are required to confirm this.

### 5.2 Implications and future work

This work set out to find cases of late-time radio re-brightening in the pilot surveys VAST-P1 and RACS-low. These early results from the pilot phase have demonstrated the promising potential for ASKAP to find sources of late-time emission or place limits on late-time CSM interaction with ejected shells from earlier mass-loss episodes – see Fig. 8. For example, we see that SN 2003bg and SN 2016coi have extremely fast outflow velocities, as expected for stripped-envelope SNe (Bietenholz et al. 2021). But we also find that the mass-loss rates for SN 2004dk and SN 2012ap at late times are larger than predicted by Smith (2014). This is a relatively unknown phase space that ASKAP is helping to fill.

Detections of these CCSNe re-brightening events provide additional examples of dense CSM inhomogenities resulting from distinct periods of extreme mass-loss, breaking the standard model constant CSM density structure. While recent results continue to support the CSM–shock interaction interpretation of late-time SNe re-brightening (e.g. DeMarchi et al. 2022; Sfaradi et al. 2024), alternative explanations – like pulsar-wind nebulae or off-axis jets – have also been suggested as central emission engines (e.g. Stroh et al. 2021; Rizzo Smith, Kochanek & Neustadt 2023).

Future work on this topic will be aided by the VAST transient detection pipeline (Pintaldi et al. 2022), which uses a streamlined source matching process across epochs to generate variability parameters used to identify sources of interest. Specifically, variables are identified based on the variability threshold and modulation index defined by Mooley et al. (2016a).

Three SNe from our sample were included in this VAST pipeline and their variability metrics were reasonably consistent with our interpretation of the sources, namely: SN 1996aq is undergoing a period of re-brightening which is slowly declining but difficult to model because the flux density variations are on the same order of magnitude as the errors. This source did not meet the pipeline's variability thresholds. SN 2012dy is undergoing a period of re-brightening that is varying on larger scales with smaller errors, with the appearance of two distinct peaks followed by a gradual decline; and still appears to be undergoing some interaction. This source passes the pipeline's 95 per cent variability confidence threshold but does not attain a sufficient modulation index; this only selects highly variable sources with an equivalent fractional flux density variation of three. While we do detect late-time radio emission from SN 2017gmr, its variability appears to be consistent with scintillation around the SELAVY$5\sigma$ cut-off. This source was not picked up by the Pintaldi et al. transient pipeline and is a good example of its ability to ignore a false positive.

SN 2013bi is another example of a false positive from our original selection process. This CCSN has almost no additional information besides its optical discovery (Jin et al. 2013). It was detected by RACS-low ~6 yr after discovery, and was faintly visible in VLASS several days later (Gordon et al. 2020), but SN 2013bi has not been observed since. Leading up to the public release of the RACS-low data, Hale et al. (2021) noted that a decreased resolution – due to an extended point spread function (PSF) in the observation of certain fields – may have produced some erroneous SELAVY detections of objects with neighbouring sources in our search.

These fields were re-observed to create a reliable catalogue with more uniform resolution and SN 2013bi was observed in one such field. In the updated observation, as in the more recent 1.365 GHz RACS survey (RACS-mid; Duchesne et al. 2023), there is significant emission from the host galaxy. Therefore we do not consider the original RACS-low flux density value reliable, as it may be confused with the extended emission. Given the sparsity of available radio detections, we do not show a light curve or calculate the variability metrics for SN 2013bi.

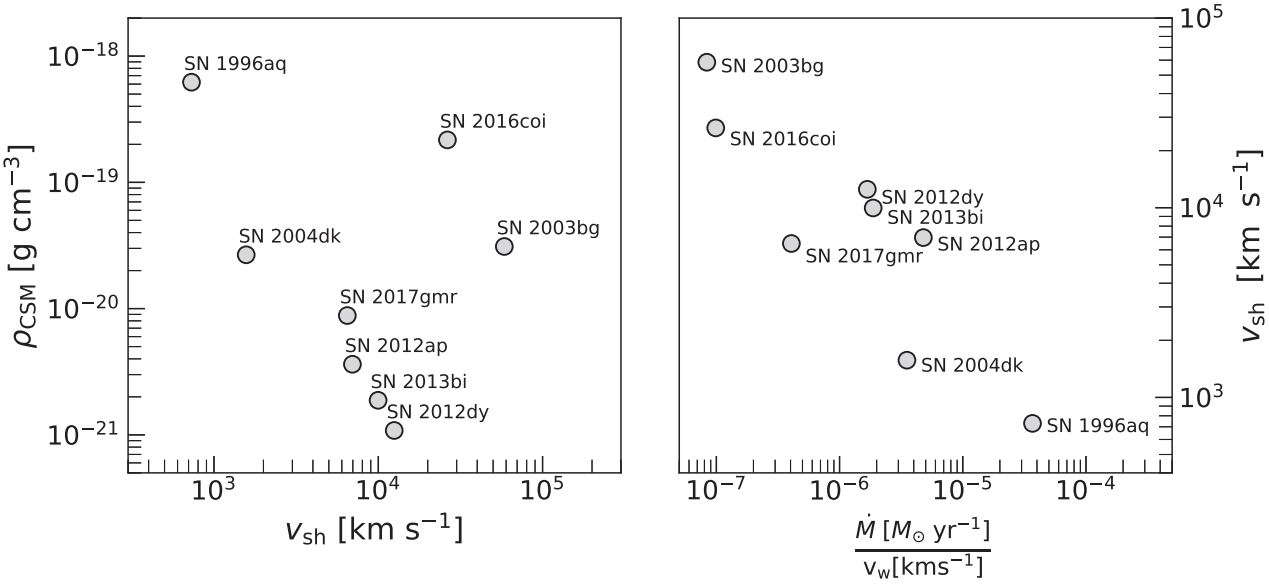


**Figure 8.** We calculate the CSM density and mass-loss rate with equations (2) and (3) for each CCSN at its respective peak flux density. *Left*: CSM density $\rho_{CSM}$ as a function of the shock velocity. *Right*: shock velocity compared to the mass-loss rate, noting that $\dot{M}$ is scaled by the wind velocities 10 and 1000 km s$^{-1}$ for Type II and Type Ib/c SNe, respectively.

## 6 SUMMARY

In this work, we have demonstrated the general ability to detect late-time SN re-brightening events with VAST.

VAST-P1 observed the complete 5131 deg$^2$ pilot survey region four times and nominally identified 29 CCSNe and five real late-time SNe re-brightening events. The full VAST survey is observing a larger region of $\sim$ 9500 deg$^2$ at an approximately bimonthly cadence over four years. A scaled estimate suggests that VAST will detect $\sim$ 640 CCSNe and $\sim$ 110 late-time SNe re-brightening events with luminosities of $L_\nu \sim 10^{29}$ erg s$^{-1}$ Hz$^{-1}$ or greater. This estimate makes the simplifying assumption of uniform source density over the survey region.

This approach may also be useful in identifying orphan afterglow events from long-duration GRBs, which are often observed to be accompanied by a Type Ic broad-lined CCSN (particularly in the local Universe). For a review of the GRB–SN connection, see Cano et al. (2017). While recent studies have shown that unbiased ASKAP surveys are now sensitive enough to detect radio emission from known GRBs (Leung et al. 2021) and find strong orphan afterglow candidates (Leung et al. 2023), the discovery of late-time supernova-powered re-brightening expected in these GRB–SN events (e.g. Barniol Duran & Giannios 2015) remains elusive due to the scarcity of late-time (decades post-burst) follow-up. The method demonstrated in this work provides a promising avenue for discovering late-time re-brightenings from GRB–SN events, which has implications for our understanding of the progenitors of GRBs, orphan afterglow searches, and constraining their true population rate.

VAST can also be used to identify and study late-time re-brightening in other classes of transients like TDEs (Anumarlapudi et al. 2024). Additionally, VAST can be used to monitor long-term variability in active galactic nuclei, as well stellar emission (Pritchard et al. 2024).

## ACKNOWLEDGEMENTS

KR thanks the LSST-DA Data Science Fellowship Program, which was funded by LSST-DA, the Brinson Foundation, and the Moore Foundation. Their participation in the programme has benefited this work. KR would like to acknowledge the help of Gemma E. Anderson and Lucinda Lilley for their helpful advice and insightful discussion. KR and RJA also thank Joshua Pritchard for his help in the early stages of this project. AH is grateful for the support by the United States-Israel Binational Science Foundation (BSF grant 2020203) and by the Sir Zelman Cowen Universities Fund. This research was supported by the Israel Science Foundation (grant no. 1679/23). DLK was supported by National Science Foundation (NSF) grant AST-1816492.

We thank the Mullard Radio Astronomy Observatory for carrying out the AMI–LA observations.

The Australia Telescope Compact Array is part of the Australia Telescope National Facility which was funded by the Australian Government for operation as a National Facility managed by CSIRO. We acknowledge the Gomeroi people as the traditional owners of the Observatory site.

This scientific work uses data obtained from Inyarrimanha Ilgari Bundara/the Murchison Radio-astronomy Observatory. We acknowledge the Wajarri Yamaji People as the traditional owners of the Observatory site. CSIRO's ASKAP radio telescope is part of the Australia Telescope National Facility. Operation of ASKAP was funded by the Australian Government with support from the National Collaborative Research Infrastructure Strategy. ASKAP uses the resources of the Pawsey Supercomputing Research Centre. Establishment of ASKAP, Inyarrimanha Ilgari Bundara, the CSIRO Murchison Radio-astronomy Observatory, and the Pawsey Supercomputing Research Centre are initiatives of the Australian Government, with support from the Government of Western Australia and the Science and Industry Endowment Fund. This paper includes archived data obtained through the CSIRO ASKAP Science Data Archive, CASDA.[18]

[18] http://data.csiro.au/

## DATA AVAILABILITY

A complete tabulation of all new and archival SN data used in this work is available in machine-readable form as an online supplement to this paper.

The ASKAP data used in this paper (RACS-low and VAST-P1) can be accessed through the CSIRO ASKAP Science Data Archive (CASDA) under project codes AS110 and AS107. The ATCA data used in this paper can be accessed through the ATOA under project codes C3363 and C3442. Other auxiliary data sets can be made available upon request via email to the corresponding author.

## REFERENCES


Anderson G. E. et al., 2017, MNRAS, 466, 3648
Andrews J. E. et al., 2019, ApJ, 885, 43
Anumarlapudi A. et al., 2024, preprint (arXiv:2407.12097)
Balasubramanian A., Corsi A., Polisensky E., Clarke T. E., Kassim N. E., 2021, ApJ, 923, 32
Barbon R., Buondí V., Cappellaro E., Turatto M., 1999, A&AS, 139, 531
Barniol Duran R., Giannios D., 2015, MNRAS, 454, 1711
Becker R. H., White R. L., Helfand D. J., 1995, ApJ, 450, 559
Bietenholz M. F., Bartel N., Argo M., Dua R., Ryder S., Soderberg A., 2021, ApJ, 908, 75
Bock G., Milisavljevic D., Parrent J. T., Fesen R., Margutti R., Soderberg A., Pickering T., Kotze P., 2012, CBET, 3197
Cano Z., Wang S.-Q., Dai Z.-G., Wu X.-F., 2017, Adv. Astron., 2017, 8929054
Chakraborti S., Chandra P., Ray A., 2009, Astron. Telegram, 1974
Chakraborti S. et al., 2015, ApJ, 805, 187
Chevalier R. A., 1982, ApJ, 259, 302
Chevalier R. A., 1996, in Taylor A. R., Paredes J. M., eds, ASP Conf. Ser., Vol. 93, Radio Emission from the Stars and the Sun. Astron. Soc. Pac., San Francisco, p. 125
Chevalier R. A., 1998, ApJ, 499, 810
Clarke T. E., Kassim N. E., Brisken W., Helmboldt J., Peters W., Ray P. S., Polisensky E., Giacintucci S., 2016, in Hall H. J., Gilmozzi R., Marshall H. K., eds, Proc. SPIE Conf. Ser., Vol. 9906, Ground-based and Airborne Telescopes VI. SPIE, Bellingham, p. 99065B
Condon J. J., Cotton W. D., Greisen E. W., Yin Q. F., Perley R. A., Taylor G. B., Broderick J. J., 1998, AJ, 115, 1693
Cornwell T. J., Voronkov M. A., Humphreys B., 2012, in Bones P. J., Fiddy M. A., Millane R. P., eds, Proc. SPIE Conf. Ser., Vol. 8500, Image Reconstruction from Incomplete Data VII. SPIE, Bellingham, p. 85000L
DeMarchi L. et al., 2022, ApJ, 938, 84
Duchesne S. W. et al., 2023, Publ. Astron. Soc. Aust., 40, e034
Foreman-Mackey D., Hogg D. W., Lang D., Goodman J., 2013, PASP, 125, 306
Frieman J. A. et al., 2008, AJ, 135, 338
Gal-Yam A., 2021, AAS. Bulletin of the AAS, Internet, 423
Gordon Y. A. et al., 2020, Res. Notes Am. Astron. Soc., 4, 175
Grupe D., Brown P., Dong S., Shappee B. J., Holoien T., Stanek K., Prieto J. L., Margutti R., 2016, Astron. Telegram, 9088
Guillochon J., Parrent J., Kelley L. Z., Margutti R., 2017, ApJ, 835, 64
Hale C. L. et al., 2021, Publ. Astron. Soc. Aust., 38, e058
Hamuy M. et al., 2009, ApJ, 703, 1612
Hancock P. J., Charlton E. G., Macquart J.-P., Hurley-Walker N., 2019, preprint (arXiv:1907.08395)
Heger A., Fryer C. L., Woosley S. E., Langer N., Hartmann D. H., 2003, ApJ, 591, 288
Hickish J. et al., 2018, MNRAS, 475, 5677
Horesh A. et al., 2020, ApJ, 903, 132
Hotan A. W. et al., 2021, Publ. Astron. Soc. Aust., 38, e009
Jewett L. et al., 2012, CBET, 3037
Jin Z. et al., 2013, CBET, 3481
Lacy M. et al., 2020, PASP, 132, 035001
Langer N., 2012, ARA&A, 50, 107
Leung J. K. et al., 2021, MNRAS, 503, 1847
Leung J. K., Murphy T., Lenc E., Edwards P. G., Ghirlanda G., Kaplan D. L., O'Brien A., Wang Z., 2023, MNRAS, 523, 4029
Margalit B., Quataert E., 2024, preprint (arXiv:2403.07048)
Mauerhan J. C., Filippenko A. V., Zheng W., Brink T. G., Graham M. L., Shivvers I., Clubb K. I., 2018, MNRAS, 478, 5050
Mazzali P. A., Deng J., Hamuy M., Nomoto K., 2009, ApJ, 703, 1624
McConnell D. et al., 2020, Publ. Astron. Soc. Aust., 37, e048
McMullin J. P., Waters B., Schiebel D., Young W., Golap K., 2007, in Shaw R. A., Hill F., Bell D. J., eds, ASP Conf. Ser., Vol. 376, Astronomical Data Analysis Software and Systems XVI. Astron. Soc. Pac., San Francisco, p. 127
Milisavljevic D. et al., 2013, ApJ, 767, 71
Milisavljevic D. et al., 2015, ApJ, 799, 51
Mooley K. P. et al., 2016a, ApJ, 818, 105
Mooley K. P. et al., 2016b, Astron. Telegram, 9134
Moriya T. J., Groh J. H., Meynet G., 2013, A&A, 557, L2
Murphy T. et al., 2013, Publ. Astron. Soc. Aust., 30, e006
Murphy T. et al., 2021, Publ. Astron. Soc. Aust., 38, e054
Nagao T. et al., 2019, MNRAS, 489, L69
Nakano S. et al., 1996, Int. Astron. Union Circ., 6454
Pacholczyk A. G., 1970, Radio Astrophysics: Nonthermal Processes in Galactic and Extragalactic Sources. W. H. Freeman, San Francisco
Palliyaguru N. T., Corsi A., Pérez-Torres M., Varenius E., Van Eerten H., 2021, ApJ, 910, 16
Perez-Torres M., et al., 2015, in Bourke Tyler L., ed, Proceedings of Advancing Astrophysics with the Square Kilometre Array (AASKA14). Proceedings of Science, Giardini Naxos, Sicily, Italy, 60
Perley R. A., Chandler C. J., Butler B. J., Wrobel J. M., 2011, ApJ, 739, L1
Perrott Y. C. et al., 2013, MNRAS, 429, 3330
Pintaldi S., Stewart A., O'Brien A., Kaplan D., Murphy T., 2022, in Ruiz J. E., Pierfedereci F., Teuben P., eds, ASP Conf. Ser., Vol. 532, Astronomical Society of the Pacific Conference Series. Astron. Soc. Pac., San Francisco, p. 333
Prentice S. J. et al., 2016, MNRAS, 458, 2973
Pritchard J., Murphy T., Heald G., Wheatland M. S., Kaplan D. L., Lenc E., O'Brien A., Wang Z., 2024, MNRAS, 529, 1258
Pursimo T. et al., 2017, Astron. Telegram, 10717
Rajala A. M. et al., 2005, PASP, 117, 132
Rizzo Smith M., Kochanek C. S., Neustadt J. M. M., 2023, MNRAS, 523, 1474
Ruiz-Carmona R., Sfaradi I., Horesh A., 2022, A&A, 666, A82
Ryder S. D., Sadler E. M., Subrahmanyan R., Weiler K. W., Panagia N., Stockdale C., 2004, MNRAS, 349, 1093
Salas P., Bauer F. E., Stockdale C., Prieto J. L., 2013, MNRAS, 428, 1207
Sault R. J., Teuben P. J., Wright M. C. H., 1995, in Shaw R. A., Payne H. E., Hayes J. J. E., eds, ASP Conf. Ser., Vol. 77, Astronomical Data Analysis Software and Systems IV. Astron. Soc. Pac., San Francisco, p. 433
Sfaradi I., Horesh A., Fender R., Green D. A., Williams D. R. A., Bright J., Schulze S., 2022, ApJ, 933, 176
Sfaradi I. et al., 2024, A&A, 686, A129
Smartt S. J. et al., 2015, A&A, 579, A40
Smith N., 2014, ARA&A, 52, 487
Soderberg A. M., Chevalier R. A., Kulkarni S. R., Frail D. A., 2006, ApJ, 651, 1005
Soderberg A. M. et al., 2010, Nature, 463, 513
Stockdale C. J. et al., 2009, CBET, 1714
Stroh M. C. et al., 2021, ApJ, 923, L24
Terreran G. et al., 2019, ApJ, 883, 147
Valenti S., Tartaglia L., Sand D., Wyatt S., Bostroem K. A., Reichart D. E., Haislip J. B., Kouprianov V., 2017, Astron. Telegram, 10706
Weiler K. W., Panagia N., Montes M. J., Sramek R. A., 2002, ARA&A, 40, 387
Wellons S., Soderberg A. M., Chevalier R. A., 2012, ApJ, 752, 17
Wenger M. et al., 2000, A&AS, 143, 9
Whiting M. T., 2012, MNRAS, 421, 3242
Wilson W. E. et al., 2011, MNRAS, 416, 832
Wood-Vasey W. M., Aldering G., Nugent P., Chassagne R., 2003, Int. Astron. Union Circ., 8082, 1

Yaron O., Gal-Yam A., 2012, PASP, 124, 668
Yin Q. F., Heeschen D. S., 1991, Nature, 354, 130
Zwart J. T. L. et al., 2008, MNRAS, 391, 1545

## SUPPORTING INFORMATION

Supplementary data are available at *MNRAS* online.

Please note: Oxford University Press is not responsible for the content or functionality of any supporting materials supplied by the authors. Any queries (other than missing material) should be directed to the corresponding author for the article.

## APPENDIX A: ASKAP SENSITIVITY LIMIT

To obtain an upper limit on the redshift for detectable CCSNe with ASKAP, we calculated the sensitivity distance horizon using Mrk 297A, which has the highest known peak radio luminosity for an SN (Yin & Heeschen 1991, and references therein). For the VAST-P1 RMS limit $\sigma_{\rm RMS} = 0.25$ mJy beam$^{-1}$, the $5\sigma$ `Selavy` threshold results in a distance limit of:

$$D = \sqrt{\frac{3 \times L_\nu}{4\pi \times 5\sigma_{\rm RMS}}} \approx \frac{3 \times 2.43 \times 10^{29}}{4\pi \times 1.25} \approx 697.65 \text{ Mpc} \qquad \text{(A1)}$$

corresponding to a redshift of $z \approx 0.146$. For this calculation we have taken three times the radio luminosity $L_\nu \approx 2.43 \times 10^{29}$ erg s$^{-1}$ Hz$^{-1}$, which was obtained by scaling the 12.2 mJy flux density at 5 GHz to 887.5 MHz with an assumed spectral index of $\alpha = -0.7$. This figure may be used only as a conservative limit on the highest possible SN radio luminosity (Perez-Torres et al. 2015).

## APPENDIX B: FULL CANDIDATE LIST

In Table B1, we provide a complete list of the 29 CCSNe late-time radio re-brightening candidates that we identified in the ASKAP data as part of this work. The type, discovery date, and distance are taken from the OpenSNe catalogue.

**Table B1.** CCSNe identified with ASKAP detections in RACS-low and VAST-P1, arranged chronologically by discovery date.

| Name | Type | RA | Dec. | Dist. (Mpc) | Disc. (MJD) |
|---|---|---|---|---|---|
| SN 1978K | SN II | 03:17:38.6 | −66:33:04 | 4.1 | 43720 |
| SN 1987A | SN IIp | 05:35:27.9 | −69:16:11 | 0.054 | 46850 |
| SN 1996aq | SN Ic | 14:22:22.7 | −00:23:23 | 23.9 | 50312 |
| SN 2002cj | SN Ic | 15:21:20.7 | −19:51:24 | 68 | 52385 |
| SN 2002hy | SN Ic | 10:54:39.2 | −21:03:41 | 45 | 52590 |
| SN 2003bg | SN IIb | 04:10:59.4 | −31:24:49 | 19.5 | 52695 |
| SN 2004dk | SN Ib | 16:21:48.9 | −02:16:17 | 22.6 | 53216 |
| SN 2004gg | SN II | 09:46:48.7 | +16:02:46 | 87 | 53325 |
| SN 2004Q | SN II | 12:47:39.7 | −26:12:22 | 108 | 53034 |
| SN 2006bl | SN II | 15:39:50.9 | +14:11:16 | 145 | 53829 |
| SN 2006O | SN II | 01:01:20.9 | +31:30:11 | 66 | 53757 |
| SN 2007rw | SN II | 12:38:03.6 | −02:15:41 | 38.3 | 54433 |
| SN 2008bu | SN II | 16:47:24.3 | −20:08:33 | 57 | 54573 |
| SN 2008de | SN II | 15:55:24.9 | −09:41:47 | 180 | 54573 |
| SN 2008fi | SN IIb | 01:53:23.3 | +29:21:31 | 110.8 | 54704 |
| SN 2012ap | SN Ic-BL | 05:00:13.7 | −03:20:50 | 53.3 | 55967 |
| SN 2012dy | SN II | 21:18:50.7 | −57:38:42 | 45.3 | 56142 |
| SN 2013bi | SN IIp | 18:25:02.1 | +27:31:53 | 71.7 | 56375 |
| SN 2014C | SN Ib | 22:37:05.7 | +34:24:30 | 12 | 56662 |
| SN 2015co | SN II | 17:14:36.0 | +30:44:07 | 131 | 57144 |
| SN 2016coi | SN Ic-BL | 21:59:04.1 | +18:11:11 | 16.18 | 57535 |
| SN 2017ggi | SN Ib | 00:58:52.9 | −35:51:46 | 178 | 57977 |
| SN 2017gmr | SN II | 02:35:30.2 | −09:21:14 | 21.7 | 58000 |
| SN 2017hyh | SN IIb | 07:10:41.0 | +06:27:41 | 53.7 | 58062 |
| SN 2018dhp | SN II | 21:32:51.7 | −25:20:20 | 141.4 | 58309 |
| SN 2018keq | SN Ic-BL | 23:22:41.8 | +21:00:42 | 180 | 58469 |
| SN 2019arl | SN Ic | 14:47:02.0 | +11:39:16 | 133.7 | 58522 |
| SN 2019atg | SN Ic | 12:02:57.9 | −30:07:51 | 201 | 58521 |
| SN 2019cac | SN IIn | 13:50:43.9 | −02:30:23 | 213.8 | 58526 |

## APPENDIX C: CONSTANTS FROM THE LITERATURE

The constant $c_1$ is given (in cgs units) explicitly by Chevalier (1998), who cite $c_5$ and $c_6$ from Pacholczyk (1970):

$$c_1 = 6.27 \times 10^{18} \tag{C1}$$

$$c_5 = \frac{\sqrt{3}}{16\pi}\frac{e^3}{mc^2}\left(\frac{\gamma+\frac{7}{3}}{\gamma+1}\right)\Gamma\left(\frac{3\gamma-1}{12}\right)\Gamma\left(\frac{3\gamma+7}{12}\right) \tag{C2}$$

$$c_6 = \frac{\sqrt{3}\pi}{72}em^5c^{10}\left(\gamma+\frac{10}{3}\right)\Gamma\left(\frac{3\gamma+2}{12}\right)\Gamma\left(\frac{3\gamma+10}{12}\right) \tag{C3}$$

## APPENDIX D: MCMC CORNER PLOTS

We provide the corner plots of the posterior distributions for our EMCEE fitting of SN 2003bg (Fig. D1), SN 2004dk (Fig. D2), and SN 2016coi (Fig. D3). We fit the multifrequency early-time data to equation (6) and assume a spectral peak frequency at the VAST observing frequency 887.5 MHz. These plots used the default option for 0.5, 1, 1.5, and 2 sigma level contours, which respectively contain 11.8 per cent, 39.3 per cent, 67.5 per cent, and 86.4 per cent of the samples.

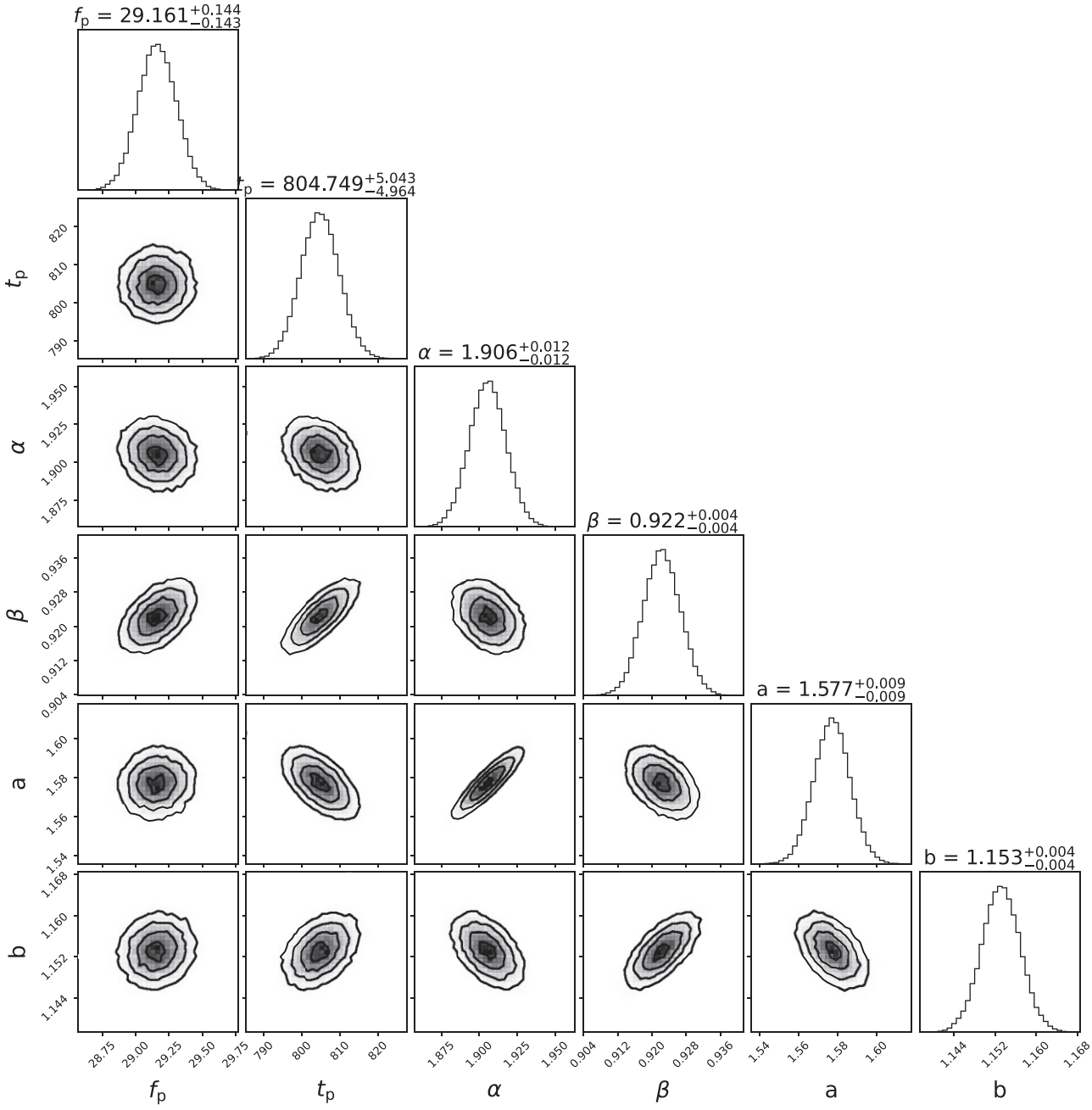


**Figure D1.** SN 2003bg corner plot of the posterior distributions for the values given in Table 3. These are obtained from our EMCEE sampling and fitting of the early-time ($\Delta t < 10^3$ d) radio data to the parametrized model given in equation (6). The grey colour scale corresponds to the density of samples.

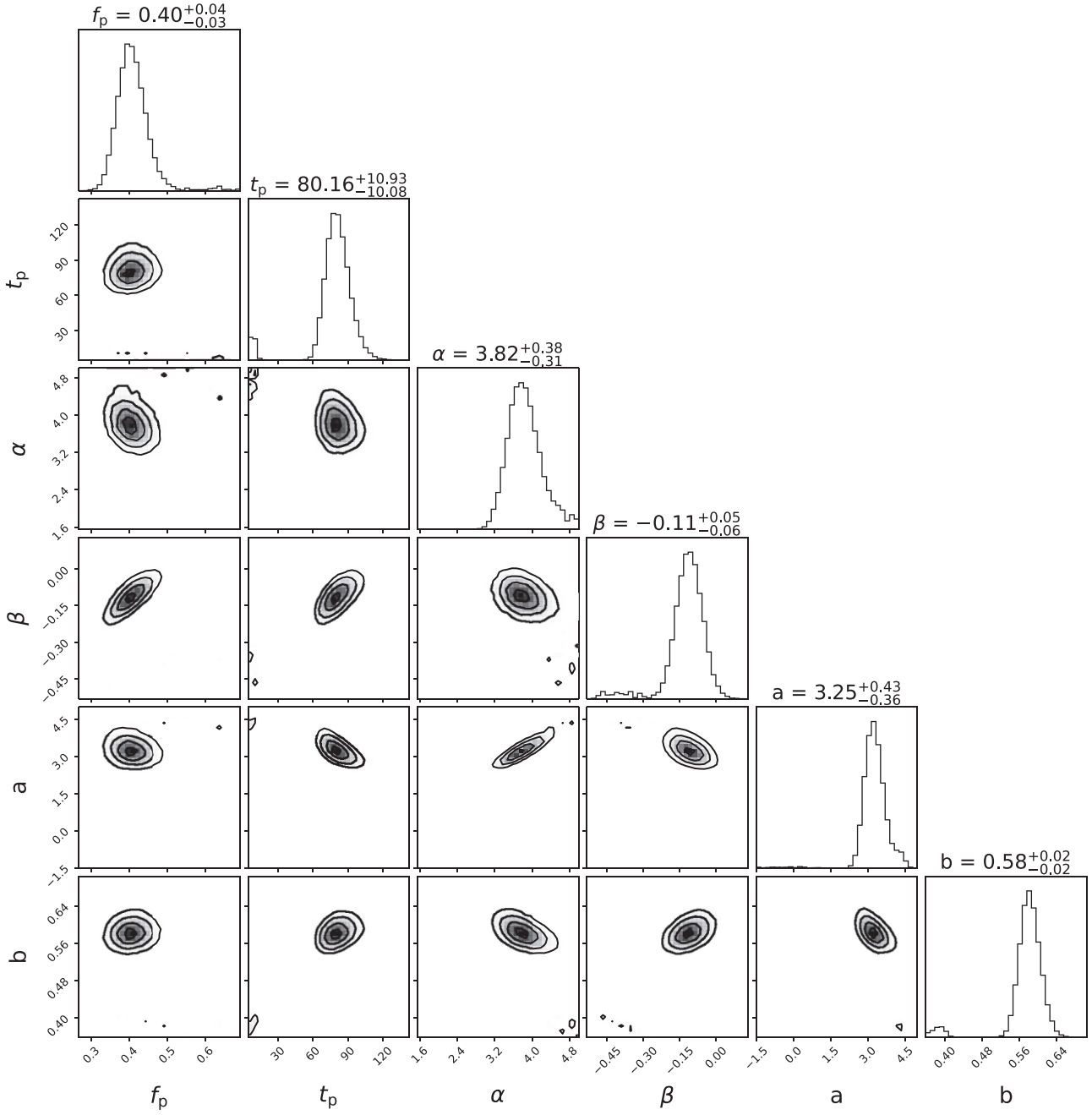


**Figure D2.** SN 2004dk corner plot of the posterior distributions for the values given in Table 3. These are obtained from our EMCEE sampling and fitting of the early-time ($\Delta t < 3 \times 10^3$ d) radio data to the parametrized model given in equation (6). The grey colour scale corresponds to the density of samples.

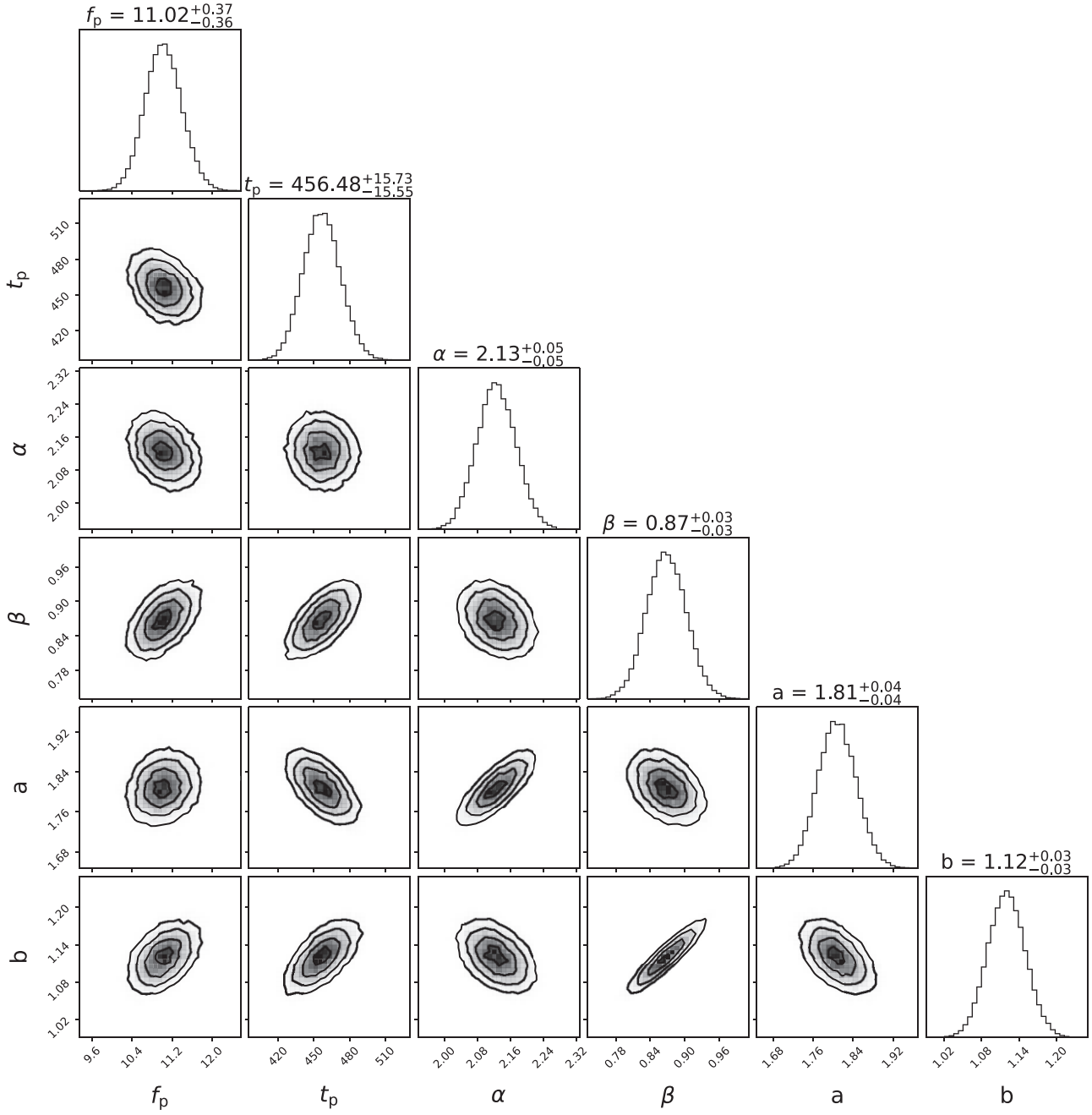


**Figure D3.** SN 2016coi corner plot of the posterior distributions for the values given in Table 3. These are obtained from our EMCEE sampling and fitting of the early-time ($\Delta t < 3 \times 10^3$ d) radio data to the parametrized model given in equation (6). The grey colour scale corresponds to the density of samples.

This paper has been typeset from a TEX/LATEX file prepared by the author.